Optimum inhomogeneity of local lattice distortions in La_2CuO_{4+y}

Nicola Poccia[a,b], Alessandro Ricci[a,c], Gaetano Campi[d], Michela Fratini[a,e], Alessandro Puri[f], Daniele Di Gioacchino[f], Augusto Marcelli[f], Michael Reynolds[b], Manfred Burghammer[b], Naurang Lal Saini[a], Gabriel Aeppli[g], and Antonio Bianconi[a,h,i,1]

[a]Department of Physics, Sapienza University of Rome, Piazzale A. Moro 2, 00185 Roma, Italy; [b]European Synchrotron Radiation Facility, B.P. 220, F-38043 Grenoble Cedex, France; [c]Deutsches Elektronen-Synchrotron DESY, Notkestraße 85, D-22607 Hamburg, Germany; [d]Institute of Crystallography, CNR, Via Salaria Km 29.300, Monterotondo Stazione, Roma I-00015, Italy; [e]Fermi Center, Piazzale del Viminale, 00187 Roma, Italy; [f]Istituto Nazionale di Fisica Nucleare, Laboratori Nazionali di Frascati, P.O. Box 13, 00044 Frascati, Italy; [g]London Centre for Nanotechnology and Department of Physics and Astronomy, University College London, 17–19 Gordon Street, London WC1H 0AH, United Kingdom; [h]Rome International Centre for Materials Science Superstripes (RICMASS), Via dei Sabelli 119A, 00185 Roma, Italy; and [i]Mediterranean Institute of Fundamental Physics, Via Appia Nuova 31, 00040 Marino, Italy

Edited by T. H. Geballe, Stanford University, Stanford, CA, and approved August 7, 2012 (received for review May 21, 2012)

Electronic functionalities in materials from silicon to transition metal oxides are, to a large extent, controlled by defects and their relative arrangement. Outstanding examples are the oxides of copper, where defect order is correlated with their high superconducting transition temperatures. The oxygen defect order can be highly inhomogeneous, even in optimal superconducting samples, which raises the question of the nature of the sample regions where the order does not exist but which nonetheless form the "glue" binding the ordered regions together. Here we use scanning X-ray microdiffraction (with a beam 300 nm in diameter) to show that for La_2CuO_{4+y}, the glue regions contain incommensurate modulated local lattice distortions, whose spatial extent is most pronounced for the best superconducting samples. For an underdoped single crystal with mobile oxygen interstitials in the spacer La_2O_{2+y} layers intercalated between the CuO_2 layers, the incommensurate modulated local lattice distortions form droplets anticorrelated with the ordered oxygen interstitials, and whose spatial extent is most pronounced for the best superconducting samples. In this simplest of high temperature superconductors, there are therefore not one, but two networks of ordered defects which can be tuned to achieve optimal superconductivity. For a given stoichiometry, the highest transition temperature is obtained when both the ordered oxygen and lattice defects form fractal patterns, as opposed to appearing in isolated spots. We speculate that the relationship between material complexity and superconducting transition temperature T_c is actually underpinned by a fundamental relation between T_c and the distribution of ordered defect networks supported by the materials.

granular superconductors | multiband superconductivity in density wave metals | scale-free heterogeneity | imaging phase separation | X-ray illumination

Defects associated with lattice instabilities in solids are at the heart of many of their useful properties (1–3), including their electrical conductivity. For example, before the discovery of high-temperature superconductivity (HTS) in the cuprates, the search for new superconductors was influenced by the observation that the materials, such as Nb_3Al ($T_c = 19$ K), Nb_3Ga ($T_c = 20$ K), and Nb_3Ge ($T_c = 23$ K) (4), with the highest transition temperatures at the edge of structural instability. Since then, lattice instabilities have been proposed to favor HTS (5). Indeed, the search for electronic-lattice instabilities of local structure in copper oxides was a driving idea for the discovery of HTS in the pseudo-ternary oxide $La_{2-x}Ba_xCuO_4$ (6) and it was soon proposed that these materials were intrinsically phase separated (7). This was confirmed in La_2CuO_{4+y}, the simplest superconducting Cu oxide (with mobile oxygen interstitials) at the insulator to metal transition at very low doping (8). Further experiments also revealed different phase segregation in the optimum-doping regime (9). The key role of lattice complexity follows because the critical temperature in all known HTS superconductors increases in compounds made of an increasing number of atomic elements as shown in Fig. 1. The lattice complexity of superconducting copper oxides was neglected by most popular theories of high T_c superconductivity, while percolative theories for granular superconductors were invoked because of the relevance of lattice disorder for electronic properties (10).

Although surface defects, including their correlation with electronic properties, have long been investigated by surface-sensitive techniques such as scanning tunneling microscopy (11), bulk defect ordering has only recently become accessible. Here the important advance has been a novel experimental method taking advantage of synchrotron radiation focusing techniques: scanning X-ray microdiffraction. It has been used for imaging phase separation in the real space in cuprates, focusing on the self-organization of defects (12). A recent surprise has been that even for "optimal" samples in a single family, the ordering of oxygen interstitials is highly inhomogeneous (12). Nonetheless, while the best annealing protocol (13) in this instance did not yield homogeneous defect ordering, it did yield the most connected "fractal" network, thus suggesting that better superconductivity ($T_c = 40$ K) is due to percolation of regions with the best ordering of interstitials. Defect growth and annealing processes, in fact, determine the quality of the superconductivity through either reduction of their population or complex self-organization (14, 15). The unanswered question concerns the nature of the medium hosting the regions with ordered interstitials. This is significant, as it will play a key role in determining many generic properties, from mechanical and chemical stability to the electrical characteristics, both in the superconducting and normal states of many cuprates that do show the ordering of mobile interstitials and other defects during sample preparation. An example of such a property is the often-observed linear relation between electrical resistivity and temperature, which could have an intrinsic, exotic origin in many-body physics but could also be specific to an inhomogeneous mixture.

For many years the dominant theories of HTS have considered a stoichiometric CuO_2 layer and have neglected the key role

Author contributions: N.P., A.R., G.C., M.F., N.L.S., A.B., and G.A. performed the experiments and followed the data analysis; N.P., A.P., D.d.G., and A.M. did the transport measurements; M.R. and M. B. provided the XRD station at ESRF; A.B., G.A., N.P., M.F., G.C., and A.M. planned the experiment and the data analysis and together wrote the paper.

The authors declare no conflict of interest.

This article is a PNAS Direct Submission.

Freely available online through the PNAS open access option.

[1]To whom correspondence should be addressed: antonio.bianconi@roma1.infn.it.

This article contains supporting information online at www.pnas.org/lookup/suppl/doi:10.1073/pnas.1208492109/-/DCSupplemental.

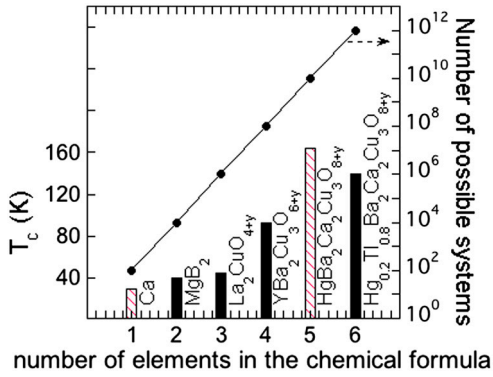

Fig. 1. The maximum superconducting critical temperature, discovered so far by material research, increases by increasing the lattice complexity. The maximum critical temperature at ambient pressure (sold bars) and high pressure (dashed bars) in systems made by a single element (Ca under pressure) and two elements (magnesium diboride) and copper oxides with multiple elements in the chemical formula.

of lattice effects (16, 17), even if the $[CuO_2]_\infty$ layers are intercalated by a variety of defective oxide AO layers (A=La, Ba, Sr, Ca, Y, Hg or Rare earths) with a large tolerance factor (18) or misfit strain (19, 20) and a large number of oxygen interstitials or defects. The lattice misfit induces tilting and corrugation of the $[CuO_2]_\infty$ layers and structural phase transitions going from I4/mmm (high temperature tetragonal), Bmab, Pccn, and Fmmm (low temperature orthorhombic, LTO) to $P4_2/ncm$ (low temperature tetragonal) in systems like La_2CuO_4 (21).

Lattice effects, also leading to inhomogeneous internal strains in perovskite manganites with fixed hole concentrations, are well established and have been connected with their colossal magnetoresistance (22–24). It is therefore worth asking whether strain inhomogeneities are also an important feature of cuprates, where they could lead to apparent phase segregation (23, 24), inducing peculiar transport properties where the self-organization associated with long-range strain interactions could even induce electronic granular networks (25). Our recent discovery (12) that better superconductivity appears with "optimal inhomogeneity" (26) of oxygen defect (O*i*) ordering opens the question of the nature of the remaining disordered medium, the topic of the present paper. The separation into an ordered network and a strained embedding medium provides a basis for the two electronic components (27–29) which have been proposed as the key feature for certain theories of high temperature superconductivity (30–32).

The local lattice distortions of the CuO_2 planes (33–37) provide another kind of ordered defect. In several doped cuprates, they yield a characteristic incommensurate superstructure with the specific wavevector $0.21\mathbf{b}*$ (38–46). Recent scanning tunneling microscopy work has clearly shown that the local lattice distortions of the CuO_2 plane induce a spatial modulation of the gap (11). The incommensurately modulated local lattice distortions (LLD) are a type of static charge density wave (CDW) established in nanoscale regions, whose size is indicated by the widths of diffuse X-ray satellites (37–45). Here we use X-ray microscopy to show that for the cuprate superconductor, La_2CuO_{4+y}, the dominant features of the embedding glue regions, where interstitials are disordered, are optimally ordered arrays of tilt defects of the copper-centered oxygen plaquets, which are the fundamental building blocks of the cuprates.

Materials

La_2CuO_{4+y} is the simplest cuprate and therefore represents an ideal venue for investigation of LLD droplets. For $0.01 < y < 0.055$, La_2CuO_{4+y} shows macroscopic phase separation between the $y1 = 0.01$ antiferromagnetic phase and the $y2 = 0.055$ superconducting phase (8, 41), where the sample shows the coexistence of two c-axis lattice constants corresponding to two competing macroscopic phases. For $y > 0.055$, La_2CuO_{4+y} shows more subtle phase separation, characterized by coexistence of two different superconducting phases with different critical temperatures, the first $T_{c1} = 15 \pm 1$ K and the second T_{c2} ranging between 27 and 38 K, even while the crystalline lattice shows no splitting of the c-axis. The first critical temperature is sensitive to O*i* ordering, and the second critical temperature is similar to that seen for $La_{2-x}Sr_xCuO_4$ (11, 46, 47).

We first investigated the competition among O*i* puddles and LLD droplets (see Table 1 for the acronyms) using a La_2CuO_{4+y} single crystal in the underdoped regime with $y = 0.06$, which corresponds to an electronic doping of 0.1 holes per Cu site. The superconducting critical temperature and the pinning properties have been characterized by ac-susceptibility experiments. The sample shows electronic phase separation into two superconducting phases with two critical temperatures, $T_{c1} = 14$ K and $T_{c2} = 27$ K (see Fig. S1), in agreement with previous studies (12, 47, 48). Synchrotron X-ray diffraction (XRD), performed at the European Synchrotron Radiation Facility (ESRF) at Grenoble, shows weak incommensurate diffuse satellites (called Q3-LLD) displaced by incommensurate wave-vector $\mathbf{q3} = 0.21\,\mathbf{b}* + 0.29\,\mathbf{c}*$ from the principal Fmmm lattice reflections (see Fig. S2) for this mono-crystal. The diffuse weak Q3-LLD satellites coexist with Q2-O*i* satellites (displaced by $\mathbf{q2} = 0.25\,\mathbf{b}* + 0.5\,\mathbf{c}*$) due to O*i* sitting at the (¼, ¼, ¼) interstitial site position (49). Q3-LLD satellites dominate and are easier to detect in underdoped samples. On the contrary, Q2-O*i* satellites are dominant at the optimum doping, for $y > 0.1$.

Results and Discussion

For our scanning X-ray microdiffraction experiments, we used the ID13 beam line of ESRF, optimized to deliver X-rays with an energy of 14 keV, focused on a 300 nm spot on the sample surface. Data were collected in the reflection geometry with a two-dimensional Fast Readout Low Noise Charged Coupled Device (FReLoN CCD) detector. We constructed images from 6370 XRD diffraction patterns, each one for a different spatial x–y position of the sample.

Fig. 2*A* and *B* contain schematics of the two coexisting structural modulations in the bc plane; the Q2-Oi and Q3-LLD respectively. Fig. 2*C* is a 3D image of O*i* puddles and LLD droplets. We may recognize the isolated puddles (cold color) and the dominant droplets phase (hot color). Fig. 2*D* demonstrates that the two signals are anticorrelated. The results show that the ordered oxygen interstitials give a granular superconducting phase with $T_{c1} = 14$ K in the underdoped regime competing with the second superconducting phase made of a distribution of droplets of LLD with $T_{c2} = 27$ K. Fig. 2*E* shows a pictorial scheme of the spatial distribution of the LLD droplets (blue circles) with a 23 nm size, deduced from the diffraction line-width (see Fig. S2), and of the large O*i* puddles (red polygons). The imaging of mesoscopic spatial inhomogeneity points clearly toward the assignment of the superconducting phases in La_2CuO_{4+y} with $T_{c11} = 14$ K in this sample and with $T_{c12} = 40$ K in the optimum doped sample (10) to the ordering of mobile O*i* forming isolated puddles and their scale-free pattern organization respectively.

Table 1. Acronyms

Acronyms	
O*i*	Oxygen interstitials sitting at the sitting at the (¼,¼, ¼) interstitial site position in the K_2NiF_4 lattice structure
Q2-Oi	Self organization of oxygen interstitials with superlattice wave-vector $\mathbf{q2} = 0.25\,\mathbf{b}* + 0.5\mathbf{c}*$
LLD	Local Lattice distortions
Q3-LLD	Self organization of local lattice distortions with superlattice wave-vector $\mathbf{q3} = 0.21\,\mathbf{b}* + 0.29\mathbf{c}*$

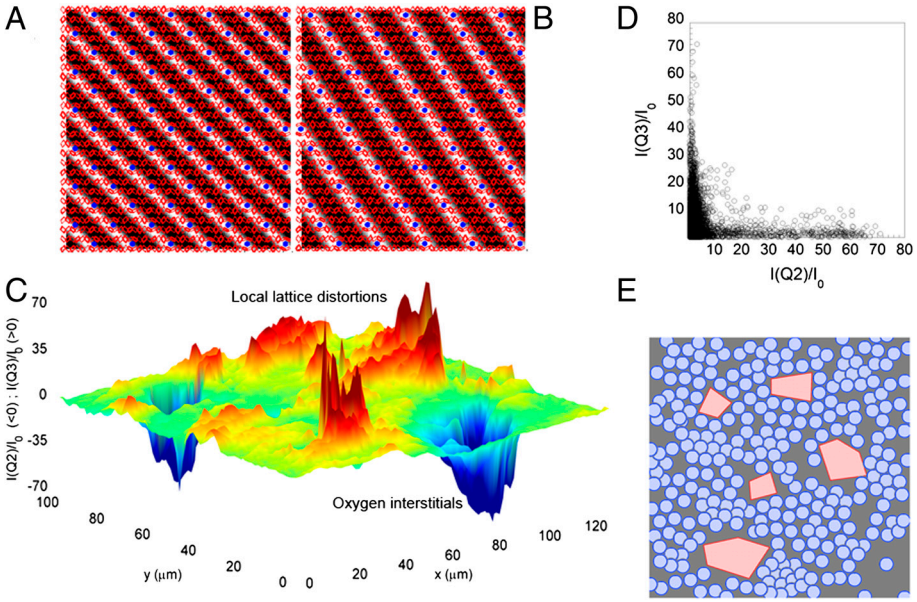

Fig. 2. The coexistence of the LLD droplets and ordered Oi puddles in different spatial locations of La_2CuO_{4+y} for y ≈0.06 as seen by scanning X-ray micro-diffraction. The pictorial view of the Q2-Oi puddles made of O*i* ordered with Q2 superstructure (*A*) and of the Q3-LLD puddles made of ordered LLD with Q3 superstructure (*B*) in the **bc** crystal plane of the Fmmm structure of La_2CuO_{4+y} **C**. The three dimensional color plot imaging the position dependence of the Q3-LLD superstructure intensity $I(Q3)/I_0$ (values >0) and of the Q2-O*i* superstructure intensity $I(Q2)/I_0$ (values <0). The scanning images show a few large disconnected Q2-Oi islands (negative blue-dark valleys) embedded in a matrix of the granular superconductor made of Q3-LLD (positive red-dark peaks). Data have been then normalized to the intensity (I_0) of the tail of the main crystalline reflections at each point (*x*, *y*). Visual inspection of both the mapping *x*–*y* position dependence of the integrated satellite peak intensity for Q2-O*i* and Q3-LLD shows that from the scale of hundreds of nanometers to micrometers, the ordered O*i* and the ordered LLD occupy distinct locations in space. The intensities of the superstructure satellites due to Q3-LLD and Q2-O*i* ordering have been integrated over square sub-areas of the images recorded by the CCD detector in reciprocal-lattice units (r.l.u.). (*D*) The Q3-LLD superstructure intensity $I(Q3)/I_0$ and of the Q2-O*i* superstructure intensity $I(Q2)/I_0$ are plotted as a function of each other. The resulting plot indicates a high degree of anti-correlation between the two type of domains characterized by different superstructures. (*E*) The schematic view of the spatial distribution of the LLD droplets (blue circles) and the ordered O*i* puddles (red polygons). The grey backgrounds are regions of the sample where neither droplets or puddles are present.

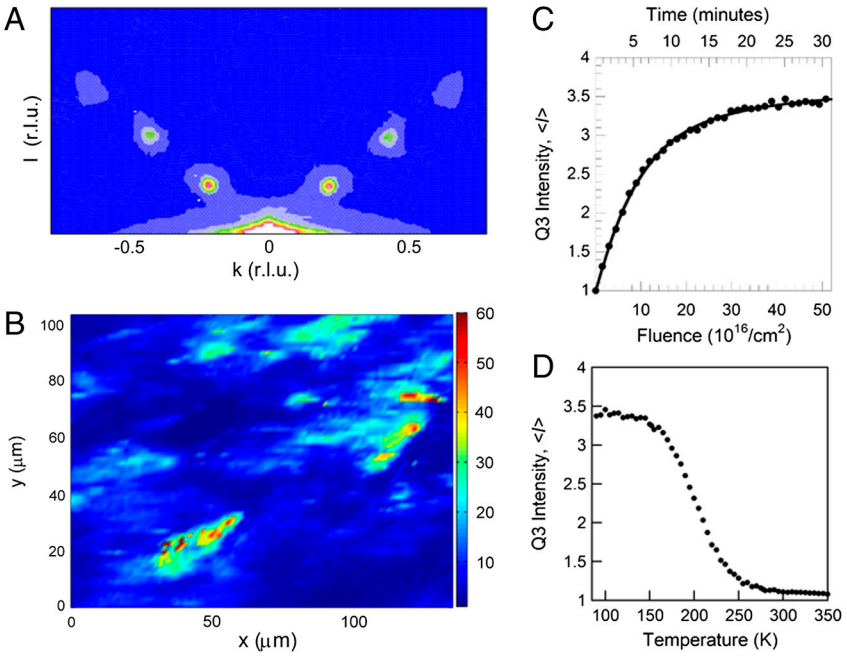

Fig. 3. (*A*) The CCD image of the Q3-LLD satellite in the b*–c* plane near the main Fmmm reflections of the underdoped La_2CuO_{4+y} single crystal, after the removal of the Q2-O*i* satellite by rapid quenching after heating the sample above 350 K. Crystals are cooled to liquid nitrogen temperatures (as low as 85 K) with a 700 series Oxford Cryosystems cryocooler. (*B*) The position dependence of the Q3-LLD superstructure intensity $I(Q3)/I_0$ in the 2D color plots after the removal of the Q2-O*i* superstructure intensity $I(Q2)/I_0$, by thermal annealing. (*C*) The intensity of the Q3-LLD XRD reflections is plotted as function of fluence ϕ or time for constant X-ray flux. The surface is illuminated by a X-ray flux $\phi_{P(0.1\,nm)} = 5.10^{14}\ N_P \cdot s^{-1}\,cm^{-2}$ keeping the temperature constant at 85 K. (*D*) The temperature evolution of the Q3-LLD satellite intensity in the range of 85 to 350 K collecting images every 2 K. The time evolution experiment has been carried out at the Elettra storage ring in Trieste. The X-ray beam, emitted by the wiggler source, was monochromatized at the 0.1 nm wavelength by a Si(111) double crystal monochromator and focused on the sample surface at the X-ray diffraction beamline (XRD1).

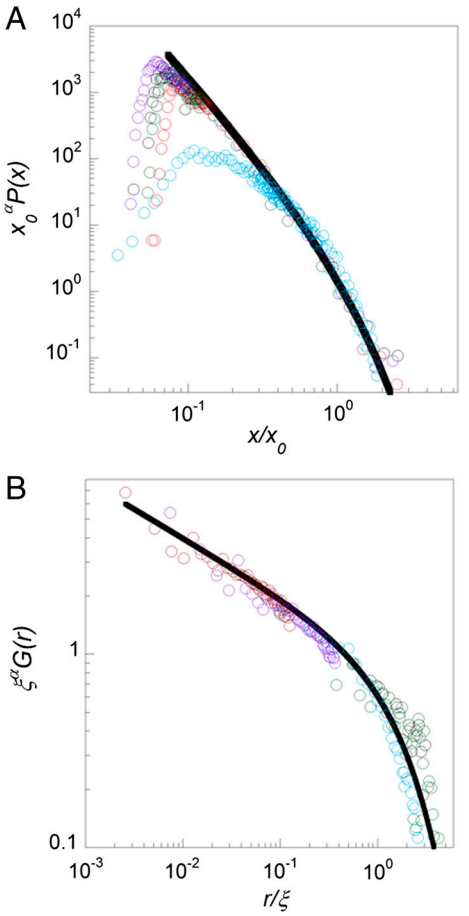

Fig. 4. (*A*) The probability distributions, P(x), of the Q3-LLD XRD intensity $x = I(Q3)/I_0$ for single crystals of electrochemically doped La_2CuO_{4+y} from the underdoped state ($y = 0.06$) to the optimum doping range, $0.1 < y < 0.12$. The curves follow a power law distribution $P(x) \propto x^{-\alpha} \exp(-x/x_0)$ with a variable exponential cut-off x_0. The curves $x_0^{\alpha}P(x)$ of all samples as a function of x/x_0 collapse on the same curve. (*B*) The spatial correlation function, G(r), of the Q3-LLD XRD follows a power law distribution $G(r) \propto r^{-\eta} \exp(-r/\xi)$. The correlation length ξ varies from 30 to 140 μm increasing with the doping range of the material investigated. The curves $\xi^{\alpha}G(r)$ of all samples as a function of r/ξ collapse onto the same curve.

We have been able to obtain a sample showing only Q3-LLD satellites by disordering the O*i* via heat treatments (11, 12) as shown in Fig. 3. We increased the sample temperature above the O*i* order-to-disorder temperature—i.e., 350 K—followed by a rapid quench below 200 K. In such a way, O*i* remains frozen in a disordered state and the Q2-O*i* diffraction peaks, as measured by the CCD area detector, are completely missing (Fig. 3*A*). Fig. 3*B* is the scanning X-ray microdiffraction image of the pattern of LLD droplets in this sample with $T_{c2} = 27$ K.

To identify how LLD droplets can arise, we carried out experiments of photo-induced effects at the Trieste synchrotron radiation facility Elettra (13). The X-ray beam spot size was 200 μm^2 on the sample surface, and the flux (defined as the number of photons hitting the sample surface per second per unit area) $\Phi_{P(0.1\ nm)} = 5 \times 10^{14}\, N_{P(0.1\ nm)} s^{-1}\, cm^{-2}$ corresponds to a power density of 1 $W\,cm^{-2}$ on the sample surface. The X-ray photon beam is at the same time a pump and probe excitation of a surface layer of about 1.5 μm. The effect of continuous illumination corresponds to photoexcitation in which the state-changing rate is proportional to the intensity of the radiation. Therefore, the physical state of the system is controlled by the fluence $F_{P(0.1\ nm)}(N_{P(0.1\ nm)} \cdot cm^{-2}) = \Phi_P \cdot t$. The sample was kept at constant temperature $T = 85$ K where the O*i* are frozen (12, 13) in the disordered glassy phase of the quenched sample. Fig. 3*C* shows the time evolution of the intensity of the Q3-LLD satellites recorded in the CCD area detector probing the (b*c*) reciprocal space at the fixed temperature of 85 K. The time evolution of the Q3-LLD XRD intensity follows the equation $I(t) \propto (1 - e^{-\frac{t}{\tau}}) \cdot t^{\gamma}$. During experiments we checked that upon doubling or halving the flux, the timescales were halved or doubled, respectively; therefore the variation of the Q3-LLD intensity is plotted as a function of the fluence. The power-law regime for the droplets follows the increase of the XRD diffraction intensity, without threshold, with an exponent $\gamma = 0.1 \pm 0.02$. To determine the temperature range where the X-ray illumination stimulates the Q3-LLD ordering, we have performed a thermal cycle from 100 K to 400 K under a high flux illumination. The Q3-LLD satellite intensity as a function of the temperature obtained by heating the sample after the X-ray illumination at 85 K is shown in Fig. 3*D*. The number of ordered domains Q3-LLD, proportional to the integrated intensity of the reflections Q3-LLD, returns to its initial value after increasing the temperature above 200 K. The results are in agreement with *i*) photo-annealing of the incommensurate modulated local lattice distortions detected by electron diffraction peaks below 200 K (43); *ii*) the photoinduced variation of superconducting properties (50, 51); and *iii*) with the onset of LLD below 200 K as detected by EXAFS (45).

The LLD droplets form networks whose nature varies with superconducting critical temperature. We have used X-ray microdiffraction apparatus at the ESRF to map the evolution of the Q3-LLD satellites for five single crystals of electrochemically doped La_2CuO_{4+y}, from the underdoped state ($y = 0.06$) to the optimum doping range, $0.1 < y < 0.12$. Fig. 4*A* and *B* shows respectively the probability distribution of XRD Q3-LLD intensities and the spatial correlation function, $G(r)$, where $r = |\mathbf{R}_i - \mathbf{R}_j|$, calculated for the intensities at the spots $\mathbf{R}_k$. From the XRD mapping we have extracted the probability distribution, P(x), of the intensity I(Q3) of the reflections due to XRD Q3-LLD satellites of the main crystalline reflections, and normalized to the background, $I(Q3)/I_0$. Normalized data have been divided by the mean XRD intensity of the sample, x, and scaled using a power law with a cut-off x_0: $P(x) \propto x^{-\alpha} \exp(-x/x_0)$ with the power-law exponent $\alpha = 2.6 \pm 0.1$. All probability distributions of XRD intensities scale with the same power-law exponent α and a variable cutoff in the range from 4.5 to 15 (Fig. 4*A*). The spatial correlation function follows a power law, $G(r) \propto r^{-\eta} \exp(-r/\xi)$, with the exponent $\eta = 0.3 \pm 0.1$ and the correlation length $\xi = 30 \pm 10$ μm in the underdoped $y = 0.06$ sample with $T_c = 27$ K.

Looking at the distance-dependent intensity correlations from the underdoped to the optimum doping state indicates that the droplets self-organize in a fractal state. Fractals appear in many fields (52, 53), including all branches of materials science where new phases grow via stochastic nucleation and accretion at first-order phase transitions (54). Of course the detailed nature, including characteristic exponents, will depend strongly on the details, such as annealing protocols and strain interactions, for the particular system under consideration. For the LLD regions in La_2CuO_{4+y}, the correlation length follows a power law with an exponential cutoff which progressively grows with higher critical temperatures. Fig. 4*B* shows that G(r) for samples with T_c in the range $27\ K > T_c > 38$ K collapse onto the same curve when plotted versus r/ξ. In particular, for $30 < T_c < 35$ K, ξ is in the range of 40 to 120 μm and for $T_c = 37$ 1 K it is 140 ± 20 μm. At the same doping level, therefore, there are shorter correlation lengths for the LLD droplets than the O*i* puddles, which in the optimal case can reach even 400 μm (12, 13).

Fig. 5 shows the T_c in the range 27–38 K, measured by complex resistivity (see Figs. S3 and S4), associated with the droplet net-

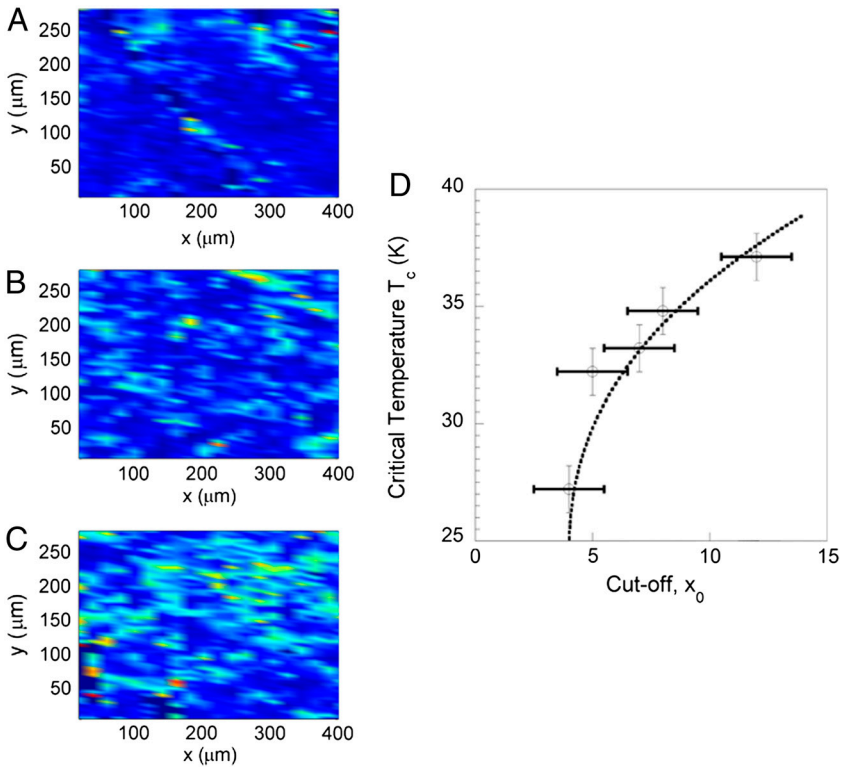

Fig. 5. (*A*, *B*, *C*) X-ray microdiffraction results for the position dependence of the Q3-LLD superstructure intensity $I(Q3)/I_0$ in the La_2CuO_{4+y} crystals with different critical temperature, T_c, 32, 34, and 37 K from A to C. The scanning XRD images show the better self organization of LLD droplets, proceeding to the higher T_c. **D**. The critical temperature T_c in the range 25 K < T_c < 37 K for five samples is plotted as a function of the cut-off parameter of the distribution of the LLD droplets density probed by the intensity distribution of the Q3-LLD superstructure satellites. Error bars in the critical temperature are of ±1 K. The dashed line is the fit with a power law curve with exponent 0.4 ± 0.05, in agreement with theoretical predictions (56) for granular superconductivity on a scale invariant network.

work, as a function of the cutoff of the probability distribution of XRD Q3-LLD intensities. The critical temperature scales with the cutoff according to a power law with an exponent 0.4 ± 0.05. This result points again toward the importance of connectivity and an optimum inhomogeneity for high critical temperature (12, 26). It is also in qualitative agreement with the theoretical prediction of the increase of T_c in a granular superconductor on an annealed complex network with a finite cutoff (55, 56). In fact, for a power-law distribution of links in a granular superconductor with an exponent $\alpha = 2.6$ the critical temperature is predicted to increase as a function of the cutoff with an exponent $3 - \alpha$, as observed experimentally.

Conclusions

We demonstrate that La_2CuO_{4+y} actually contains networks of two superconductors characterized by different ordered defects (O*i* and LLD). The best fractal behavior and superconductivity is obtained simultaneously for both O*i* and LLD order. In particular, we have provided a positive correlation between the cutoff, x_o, for scale-invariance of the LLD diffraction intensity distribution and T_c. Furthermore, the strains in the LLD droplets are correlated over the longest distances when the stresses produced over still larger distances by the ordered interstitials display their maximal correlations, a condition which also yields superconductivity with a maximum T_c. Therefore we argue that the best fractal O*i* network strains the embedding medium with LLD order the most.

Our quantitative results should be tested against theories of composite, granular superconductors proposed for cuprates (10, 14, 15, 25, 30–32, 55–62). The X-ray data indicate that these theories must take into account not only the usual superconducting proximity effects, but also the effects of the strains the two components exert on each other. It is the latter which must be ultimately responsible for the exponents α and η which we observe, and given the long-range nature of strain interactions, they cannot be accounted for within a simple near-neighbor percolation model. Our work provides a rationale for the observation of Fig. 1 showing that the main determinant of T_c is complexity of the underlying material. Indeed, having already shown that there are at least two highly relevant, coexisting networks of ordered defects in the simplest cuprate, it is quite possible that there are numbers $N > 2$ of such networks for the more complex materials. T_c then grows with N because of two effects: (*i*) the larger chances of optimal strain and Josephson (proximity) couplings with increasing N, even though the underlying nanoscale pairing propensities remain invariant, and (*ii*) the accommodation of larger doping densities in portions of samples with larger N. Our thinking suggests a clear program for future theory, taking into account random network, long-range strain and granular superconductivity concepts, and experiments exploiting X-ray microdiffraction to identify the order parameters and microstructure of these networks not only for the cuprates, but also for other complex superconductors, such as the pnictides for which analogous phase separation effects have been recently observed (63–65)

ACKNOWLEDGMENTS. We thank G. Bianconi, L.P. Gor'kov, V. Kresin, K.I. Kugel, F. Kusmartsev, G.B. Teitel'baum, V.I. Yukalov, J. Zaanen, for helpful discussions and communications. We are grateful to the ID13 beamline staff at European Synchrotron Radiation Facility (ESRF). We thank the Elettra XRD beamline staff in Trieste for experimental help and especially G. Arrighetti, L. Barba, G. Bais and M. Polentarutti. This experimental work has been carried out with the financial support of the European STREP project 517039 "Controlling Mesoscopic Phase Separation". One of the author (N.P.) would like to thank the University "La Sapienza" of Rome for providing the financial assistance for his stay at the ESRF of Grenoble.

1. Hwang HY, et al. (2012) Emergent phenomena at oxide interfaces. *Nat Mater* 11:103–113.
2. Brinkman A, et al. (2007) Magnetic effects at the interface between non-magnetic oxides. *Nat Mater* 6:493–496.
3. Dagotto E (2011) Condensed-matter physics: The conducting face of an insulator. *Nature* 469:167–168.
4. White RW, Geballe TH (1979) *Long Range Order in Solids*, eds H Ehrenreich, F Seitz, and D Turnbull (Academic, New York).
5. Gor'kov LP (1973) Contribution to the theory of the properties of the superconductors with beta-W structure. *Zh Eksp Teor Fiz* 65:1658–1676.
6. Müller KA, Bednorz JG (1987) The discovery of a class of High-Temperature superconductors. *Science* 237:1133–1139.
7. Gor'kov LP, Sokol AV (1987) Phase stratification of an electron liquid in the new superconductors. *JETP Lett* 46:420–423.
8. Jorgensen JD, et al. (1988) Superconducting phase of La_2CuO_{4+y}: A superconducting composition resulting from phase separation. *Phys Rev B* 38:11337–11345.
9. Mohottala HE, et al. (2006) Phase separation in superoxygenated $La_{2-x}Sr_xCuO_{4+y}$. *Nat Mater* 5:377–382.
10. Phillips JC (2010) Percolative theories of strongly disordered ceramic high-temperature superconductors. *Proc Natl Acad Sci USA* 107:1307–1310.
11. Slezak JA, et al. (2008) Imaging the impact on cuprate superconductivity of varying the interatomic distances within individual crystal unit cells. *Proc Natl Acad Sci USA* 105:3203–3208.
12. Fratini M, et al. (2010) Scale-free structural organization of oxygen interstitials in La_2CuO_{4+y}. *Nature* 466:841–844.
13. Poccia N, et al. (2011) Evolution and control of oxygen order in a cuprate superconductor. *Nat Mater* 15:28–59.
14. Zaanen J (2010) High-temperature superconductivity: The benefit of fractal dirt. *Nature* 466:825–827.
15. Littlewood P (2011) Superconductivity: An X-ray oxygen regulator. *Nat Mater* 10:726–727.
16. Bar-Yam Y, Egami T, Mustre-de Leon J, Bishop AR, eds. (1992) *Lattice Effects in High-T_c Superconductors* (World Scientific, Singapore).
17. Muller KA, Bussmann-Holder A, eds. (2005) Superconductivity in Complex Systems. *Structure and Bonding* (Springer, Berlin), Vol 114.
18. Bianconi A, Saini NL, Agrestini S, Castro D, Bianconi G (2000) The strain quantum critical point for superstripes in the phase diagram of all cuprate perovskites. *Int J Mod Phys B* 14:3342–3355.
19. Agrestini S, Saini NL, Bianconi G, Bianconi A (2003) The strain of CuO_2 lattice: The second variable for the phase diagram of cuprate perovskites. *J Phys A Math Gen* 36:9133–9142.
20. Bianconi A, Agrestini S, Bianconi G, Di Castro D, Saini NL (2001) A quantum phase transition driven by the electron lattice interaction gives high T_c superconductivity. *J Alloys Compd* 317:537–541.
21. Axe JD, et al. (1989) Structural phase transformations and superconductivity in La_2CuO_4. *Phys Rev Lett* 62:2751–2754.
22. Hwang HY, Cheong SW, Radaelli PG, Marezio M, Batlogg B (1995) Lattice effects on the magnetoresistance in doped $LaMnO_3$. *Phys Rev Lett* 75:914–917.
23. Dagotto E (2003) *Nanoscale Phase Separation and Colossal Magnetoresistance: The Physics of Manganites and Related Compounds* (Springer, Berlin).
24. Goodenough JB, Zhou JS (1997) New forms of phase segregation. *Nature* 386:229–230.
25. Thorpe MF, Phillips JC, eds. (2002) *Phase Transitions and Self-Organization in Electronic and Molecular Networks: Fundamental Materials Research* (Kluwer Academic Publishers, Boston), Vol 24.
26. Geballe TH, Marezio M (2009) Enhanced superconductivity in Sr_2CuO_{4-y}. *Physica C Supercond* 469:680–684.
27. Bianconi A (1994) On the Fermi liquid coupled with a generalized wigner polaronic CDW giving high T_c superconductivity. *Solid State Commun* 91:1–5.
28. Müller KA (2007) On the superconductivity in hole doped cuprates. *J Phys Condens Matter* 19:251002.
29. Haase J, Slichter CP, Williams VM (2009) Evidence for two electronic components in high-temperature superconductivity from NMR. *J Phys Condens Matter* 21:455702.
30. Gor'kov LP, Teitel'baum GB (2008) The two-component physics in cuprates in the real space and in the momentum representation. *J Phys Conf Ser* 108:012009.
31. Gor'kov LP, Teitel'baum GB (2006) Interplay of externally doped and thermally activated holes in $La_{2-x}Sr_xCuO_4$ and their impact on the pseudogap crossover. *Phys Rev Lett* 97:247003.
32. Gor'kov LP, Teitel'baum GB (2010) Spatial inhomogeneities in iron pnictide superconductors: The formation of charge stripes. *Phys Rev B Condens Matter* 82:020510.
33. Bianconi A, et al. (1996) Determination of the local lattice distortions in the CuO_2 plane of $La_{1.85}Sr_{0.15}CuO_4$. *Phys Rev Lett* 76:3412–3415.
34. Bianconi A, Lusignoli M, Saini NL, Bordet PA, Radaelli PG (1996) Stripe structure of the CuO_2 plane in $Bi_2Sr_2CaCuO_2O_{8+y}$ by anomalous X-ray diffraction. *Phys Rev B Condens Matter* 54:4310–4314.
35. Dmowski W, et al. (1995) Temperature-dependent X-ray diffuse scattering from single crystals of $La_{2-x}Sr_xCuO_4$. *Phys Rev B Condens Matter* 52:6829–6839.
36. Božin ES, Kwei GH, Takagi H, Billinge SJL (2000) Neutron diffraction evidence of microscopic charge inhomogeneities in the CuO_2 plane of superconducting $La_{2-x}Sr_xCuO_4$ ($0 \leq x \leq 0.30$). *Phys Rev Lett* 84:5856–5859.
37. Billinge SJL, Levin I (2007) The problem with determining atomic structure at the nanoscale. *Science* 316:561–565.
38. Isaacs ED, et al. (1994) Diffuse X-ray scattering from $La_{2-x}Sr_xNiO_4$ and $La_{2-x}Sr_xCuO_4$. *Phys Rev Lett* 72:3421–3424.
39. Poccia N, et al. (2011) Spatial inhomogeneity and planar symmetry breaking of the lattice incommensurate supermodulation in the high-temperature superconductor $Bi_2Sr_2CaCuO_2O_{8+y}$. *Phys Rev B Condens Matter* 84:100504.
40. Radaelli PG, et al. (1993) Structure of the superconducting La_2CuO_{4+y} phases ($y = 0.08,0.12$) prepared by electrochemical oxidation. *Phys Rev B Condens Matter* 48:499–510.
41. Radaelli PG, et al. (1994) Miscibility gap in electrochemically oxygenated La_2CuO_{4+y}. *Phys Rev B Condens Matter* 49:6239–6245.
42. Di Castro D, Colapietro M, Bianconi G (2000) Metallic stripes in oxygen doped L_2CuO_4. *Int J Mod Phys B* 14:3438–3443.
43. Gao M, Liu GD, Che GC, Zhao ZX, Peng LM (2001) Characterization of modulation structure in $La_2CuO_{4.12}$ by electron diffraction. *Phys Rev B Condens Matter* 64:224113.
44. Hammel PC, et al. (1998) Localized holes in superconducting lanthanum cuprate. *Phys Rev B Condens Matter* 57:R712–R715.
45. Lanzara A, et al. (1997) Temperature-dependent modulation amplitude of the CuO_2 superconducting lattice in $La_2CuO_{4.1}$. *Phys Rev B Condens Matter* 55:9120–9124.
46. Kremer RK, Hizhnyakov V, Sigmund E, Simon A, Muller KA (1993) Electronic phase separation in La-cuprates. *Z Phys B Condens Matter* 91:169–174.
47. Lorenz B, Li ZG, Honma T, Hor PH (2002) Intrinsic tendency of electronic phase separation into two superconducting states in $La_{2-x}Sr_xCuO_{4+\delta}$. *Phys Rev B Condens Matter* 65:144522.
48. Liu LH, Che GC (2006) T_c evolvement of thermal treated $La_2CuO_{4+\delta}$. *Physica C Supercond* 443:85–87.
49. Chaillout C, et al. (1989) Structural aspects of the phase separation in $La_2CuO_{4.032}$. *Physica C Supercond* 162–164:57–58.
50. Foster CM, Heeger AJ, Kim YH, Stucky G, Herron N (1989) Photogenerated carriers in La_2CuO_4, $YBa_2Cu_3O_{7-\delta}$ and $Tl_2Ba_2Ca_{1-x}Gd_xCu_2O_8$: Polarizability-induced pairing of polarons. *Synth Met* 33:171–183.
51. Yu G, Lee CH, Heeger AJ, Cheong SW, Fisk Z (1992) Photo-excitation of single crystals of near the metal-insulator transition. *Physica C Supercond* 190:563–568.
52. Mandelbrot BB (1982) *The Fractal Geometry of Nature* (W.H. Freeman, New York), 1st Ed, p 460.
53. Baraba'si A-L, Stanley HE (1995) *Fractal Concepts in Surface Growth* (Cambridge Univ Press, London).
54. Binder K, Kob W (2011) *Glassy Materials and Disordered Solids: An Introduction to their Statistical Mechanics* (World Scientific, Singapore), revised Ed.
55. Bianconi G (2012) Enhancement of T_c in the superconductor–insulator phase transition on scale-free networks. *J Stat Mech Theory Exp* P07021.
56. Bianconi G (2012) *Phys Rev B Condens Matter* 85:061113.
57. Kresin V, Ovchinnikov Y, Wolf S (2006) Inhomogeneous superconductivity and the "pseudogap" state of novel superconductors. *Phys Rep* 431:231–259.
58. Bishop AR (2008) HTC oxides: a collusion of spin, charge and lattice. *J Phys Conf Ser* 108:012027.
59. Kugel KI, Rakhmanov AL, Sboychakov AO, Poccia N, Bianconi A (2008) Model for phase separation controlled by doping and the internal chemical pressure in different cuprate superconductors. *Phys Rev B Condens Matter* 78:165124.
60. Pinheiro CFS, de Mello EVL (2012) Random resistivity network calculations for cuprate superconductors with an electronic phase separation transition. *Physica A* 391:1532–1539.
61. Yukalov VI, Yukalova EP (2004) Mesoscopic phase separation in anisotropic superconductors. *Phys Rev B Condens Matter* 70:224516.
62. Phillabaum B, Carlson EW, Dahmen KA (2012) Spatial complexity due to bulk electronic nematicity in a superconducting underdoped cuprate. *Nat Commun* 3:915.
63. Ricci A, et al. (2011) Nanoscale phase separation in the iron chalcogenide superconductor $K_{0.8}$ $Fe_{1.6}$ Se_2 as seen via scanning nanofocused X-ray diffraction. *Phys Rev B Condens Matter* 84:060511.
64. Li W, et al. (2011) Phase separation and magnetic order in K-doped iron selenide superconductor. *Nat Phys* 8:126–130.
65. Ksenofontov V, et al. (2011) Phase separation in superconducting and antiferromagnetic $K_{0.8}$ $Fe_{1.6}$ Se_2 probed by mössbauer spectroscopy. *Phys Rev B Condens Matter* 84:180508.

Supporting Information

Poccia et al. 10.1073/pnas.1208492109

SI Text

SI Materials Aspects. ***Susceptibility measurements.*** Experiments of the susceptibility response of the La_2CuO_{4+y} single crystal have been performed at Frascati in the LAMPS laboratory of the INFN. The susceptometer contains a gradiometer based on a bridge made by two pickup coils connected in series, wounded in the opposite sense, surrounded by a drive excitation coil. Samples are located on top of a sapphire holder slab that fits at the center of one of the two pickup coils of the bridge while the second remains empty. The coils assembly is cooled in a thermally controlled He gas-flow cryostat where a superconducting magnet operates up to 8 T. The ac driving magnetic field frequency (f) may range from 17 Hz to 1070 Hz with an amplitude from 0 to 20 G. Experiments have been performed at 107 Hz. The induced signal due to the presence of the sample has been measured by a multi-harmonic lock-in amplifier Signal Recovery model 7265 DSP. The temperature has been measured by a platinum thermometer and by a carbon resistor placed near the sample and in thermal contact with a the sapphire holder. Fig. S1 shows the magnetic measurements performed with an ac magnetic field of $H_{ac} = 5.4$. The measure has been performed warming the sample from 4.4 K

2. X-ray scanning nanodiffraction experimental setup. Scanning nanoscale diffraction experiments were performed at the ID13 beamline of the European Synchrotron Radiation Facility (ESRF), Grenoble, France. The ID13 nanobranch is specialized in the delivery of nano-focused X-ray beams for diffraction experiments. The photon source, an 18-mm period in-vacuum undulator at ESRF works in the range 12–14 KeV with the storage ring operating at 6.03 GeV in the uniform mode with a current of 200 mA. The beamline uses a Si-111 channel cut crystal monochromator cooled with liquid nitrogen. A monochromatic X-ray beam of photon energy 14 keV ($\Delta E/E = 10^{-4}$) was used, which was focused by Kirkpatrick Baez (KB) mirrors to a 300-nm spot size on the sample (full width at half maximum). A 16-bit 2D Fast Readout Low Noise charged coupled device (FReLoN CCD) detector with 2048×2048 pixels of 51×51 μm^2 was used, binned to 512 by 512 pixels. The detector was placed 60 mm behind the sample and offset. Diffraction images were obtained after correcting the 2D images for dark noise, flat field, distortion, and eventually background. The FreLoN CCD camera records the intensity I(Q3) of the satellite superstructure Q3 that correspond to the square root volume of the incommensurate domains in the selected sample surface spot (see Fig. S3). The intensity, I (Q3), is integrated over square subareas of the images recorded by the FreLoN CCD CCD detector in reciprocal-lattice units (r.l.u.) and then normalized to the intensity (I_0) of the tail of the main crystalline reflections at each point (x,y) of the sample reached by the translator. The interaction volume with the crystal of the 300-nm beam is $0.3 \times 0.3 \times 1.5 \mu m^3$.

Time- and temperature-dependent X-ray diffraction experiments. The photo-induced structural effects have been investigated by time-dependent diffraction experiments. The data have been collected on the X-ray diffraction beamline (XRD1) at the Elettra storage ring in Trieste (Italy). The X-ray beam, emitted by the wiggler source at the 2 GeV storage ring, was monochromatized by a Si(111) double crystal and focused on the sample. Crystals were cooled to liquid nitrogen temperatures (as low as 85 K) with a 700 series Oxford Cryosystems cryo-cooler. The temperature of the crystal has been monitored with an accuracy of ± 1 K. We have collected data in the reflection geometry using a FreLoN CCD detector assembly, with a photon energy of 12.4 keV and a high-flux X-ray beam available at third-generation synchrotron radiation sources. The beam size was approximately 200 μm^2. The experimental setup consists of a kappa diffractometer fully controllable from a remote computer. This experiment provides the diffraction intensity averaged over the sample surface area illuminated by the beam spot. The CCD camera records the intensity I(Q3) of the satellite superstructure Q3 (see Fig. S2). The sample oscillation around the b axis is in the range $0 < \Phi < 20°$, where Φ is the angle between the direction of the photon beam and the **a** axis. We investigated a portion of the reciprocal space recording the diffraction spots up to the maximum indexes 3, 3, 19 in the a*, b*, c* directions, respectively.

Surface resistivity. Experimental setup for single-coil inductance measurements was made on the same crystal surface as probed by X-ray diffraction (see Fig. S3). The measurement system contains a simple electronic circuit consisting of a capacitor C, connected in parallel to a spiral coil with an inductance L, and a resistance R that is placed on the sample surface. This circuit is mounted in a liquid Helium^3 cryostat (HELIOX^{3}He). In this experimental system, the sample temperature is controlled and measured by an Oxford ITC-503 temperature controller, interfaced with a computer alongside other measuring devices. A change of impedance of the LC circuit is detected as a change of resonant frequency ω and amplitude V of the oscillating signal. The LC parameters are chosen to set ω at 2–4 MHz, which is within the range of optimum operation of the oscillator. The very high sensitivity of the method arises from the strong mutual inductance between sample and coil in the single-coil geometry, in addition to the very high frequency stability of the oscillator. The single-coil inductance technique, nondestructive and contactless, enables us to measure the complex conductivity of the same crystal surface investigated by x-ray diffraction. A miniaturized pancake coil with a 0.5 mm diameter has been used. The temperature variation of the resonant frequency $\omega(T) = \sqrt{\frac{1}{L(T)C} - \frac{R(T)^2}{L(T)^2}}$ provides a measure of the temperature variation of the coil inductance $L = L_o - \pi\mu_o \int_0^\infty \frac{M(\gamma)}{1+2\gamma\lambda\coth(d/\lambda_L)} d\gamma$ where $M(\gamma)$ is the mutual inductance between coil and sample at a given wave number γ. Therefore the measured $(\omega_0/\omega)^2$, where ω_0 is the reference frequency of the coil measured in the proximity of non-superconducting copper metal, is a measure of the surface resistivity at frequency ω, proportional to the London penetration depth λ_L. Surface resistivity of the $La_2CuO_{4.1}$ samples quenched at different stages of the LLT Q3 puddles growth (see Fig. S4).

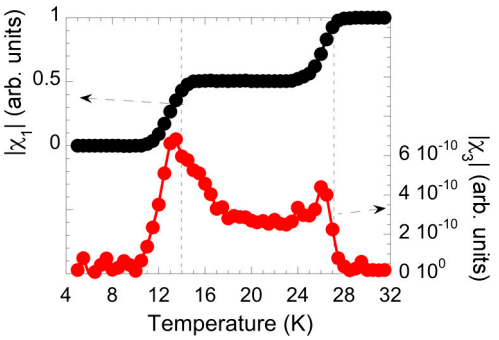

Fig. S1. The first harmonic (real part) $|\chi_1{}'|$ and the modulus of the third harmonic of ac susceptibility $|\chi_3|$ of the underdoped $La_2CuO_{4.06}$ sample showing two superconducting transition temperatures: $T_{c11} = 14 \pm 1$ K, and $T_{c2} \approx 27 \pm 1$ K.

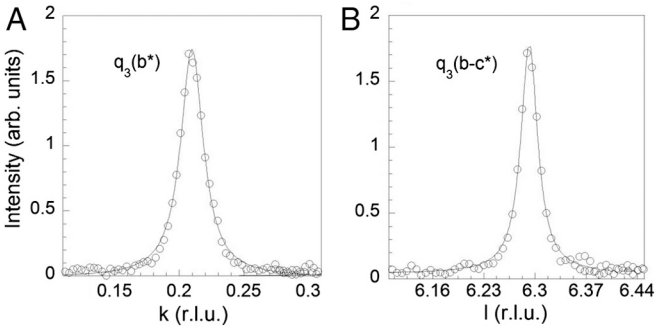

Fig. S2. Scans along the $Q = (0, k, 6 + \Delta k)$ (left) and along the $Q = (h, 0, 6 + \Delta l)$ (right) due to the diffuse scattering peaks of Q3. The intrinsic broadening of the diffuse Q3-LLD satellites dominates over the instrumental broadening, therefore, from the full width at half maximum (FWHM) corrected by the instrumental resolution, we obtained that the droplets have a maximum size of 23.5 ± 3.5 nm in the b-axis direction; i.e., about 9 ± 1 Q3-LLD oscillations in the b direction and a maximum length of 38.5 ± 5 nm along the c-axis, made of 8.5 ± 1 Q3-LLD oscillations.

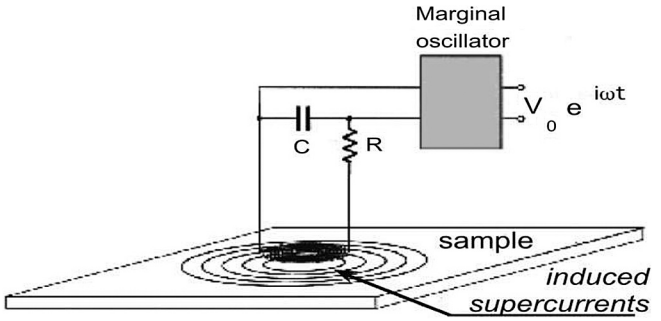

Fig. S3. Block diagram of the experimental setup for surface resistivity showing the coil–sample arrangement, the LC circuit, and the marginal oscillator.

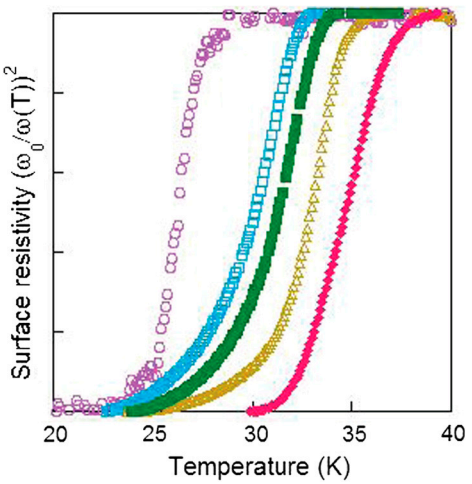

Fig. S4. Temperature-dependent complex surface resistivity of doped La_2CuO_{4+y} superconducting crystals. We used a single-coil inductance method recording $(\omega_o/\omega(T))^2$, where $\omega(T)$ is the resonance frequency of an *LC* circuit, *L* is the inductance of the submillimetre coil placed near the surface of the superconducting sample, and ω_o is the reference resonance frequency for a non-superconducting sample. The red-filled squares, yellow empty triangles, green-filled squares, cyan empty squares, and purple empty circles correspond respectively to samples with $T_c = 37.1$; 34.8; 33.2; 32.4; and 27.2 K. Error bars in the critical temperature are of ± 1 K.